Agrociencia

# AL-BIRUNI EARTH RADIUS OPTIMIZATION FOR ENHANCED ENVIRONMENTAL DATA ANALYSIS IN REMOTE SENSING IMAGERY

Sridharan **Sivasubramanian**[1], Sam Kumar **Gopalsamy Venkatesan**[2], Tamilvizhi **Thanarajan**[3], Surendran **Rajendran**[4*]

[1]University College of Engineering, Department of Computer Science and Engineering. Thirukkuvalai, Nagappattinam, India. 610204.
[2]Koneru Lakshmaiah Education Foundation. Department of Computer Science and Engineering. Vaddeswaram, Andhra Pradesh, India. 522302.
[3]Panimalar Engineering College. Department of Computer Science and Engineering. Chennai, India. 600123.
[4]Saveetha Institute of Medical and Technical Sciences. Saveetha School of Engineering, Department of Computer Science and Engineering. Chennai, India. 602105.
* Author for correspondence: surendranr.sse@saveetha.com

**Citation:** Sivasubramanian S, Gopalsamy Venkatesan SK, Thanarajan T, Rajendran S. 2025. Al-Biruni Earth Radius Optimization for enhanced environmental data analysis in remote sensing imagery. **Agrociencia.** https://doi.org/ 10.47163/agrociencia.v59i5.3380

**Editor in Chief:**
Dr. Fernando C. Gómez Merino

Received: December 23, 2024.
Approved: July 27, 2025.
**Published in Agrociencia:** August 01, 2025.



## ABSTRACT

Environmental observation techniques that use remote sensing (RS) scene image categorization play an important role in the widespread use of RS data in both civil and military domains. However, the characteristics of an RS dataset, such as its increased dimensionality and limited number of available labeled examples, present practical and scientific difficulties when attempting RS image classification. As a result of the significant advancements in RS scene image classification with deep transfer learning, there are now numerous opportunities for scientific studies and research. This study focuses on the implementation of the Al-Biruni Earth Radius Optimization with deep transfer learning-based scene image classification (AERODTL-SIC) technique on RS images. The proposed AERODTL-SIC method utilized a deep convolutional neural network-based SqueezeNet method to extract features from RS images in order to determine the various types of scenes. The AERODTL-SIC technique exploits a deep autoencoder neural network (DAENN) for scene image classification. The parameters for the DAENN model were perfectly selected using the AERO model, resulting in improved classification performance. An extensive ranging simulation result was obtained on the benchmark RS image database to demonstrate the efficiency of the AERODTL-SIC algorithm, outperforming current methodologies on a variety of performance metrics.

**Keyword:** remote sensing data images, information extraction, image classification.

## INTRODUCTION

Remote sensing image (RSI) exploration involves the study and interpretation of the semantic content of the Earth's surface. The increasing availability of high-resolution RSIs has facilitated the expansion of various research domains, including geographic

image retrieval, automated target detection, and environmental image classification (Xue *et al*., 2022; Reddy and Vimal, 2024). However, the classification of RSIs remains challenging due to the diversity of ground objects and their complex attributes, such as variation in position, scale, and color, in contrast to usual imagery (Song *et al*., 2019). Traditional object-level and pixel-level models are insufficient to accurately categorize these diverse objects, especially with the growing resolution of RSIs (Surendran *et al*., 2023a).

There is a growing emphasis on understanding the meaning and global content of RSIs (Xu *et al*., 2020). Recent efforts have focused on environmental-level analysis by categorizing each RSI patch into a semantic class (Shi *et al*., 2022). However, classifying RSIs remains challenging due to the diversity and complexity of ground objects, which vary significantly in position, size, and color compared to conventional imagery (Song *et al*., 2019). Traditional object-level and pixel-level models are insufficient to accurately classify this wide variety of objects, especially given the ever-increasing resolution of RSIs (Surendran *et al*., 2023b).

The classification of extraction types is also a complex challenge, particularly when transitioning to object- and environment-level analyses (Tamilvizhi *et al*., 2022). This complexity is intensified by the intricate spatial arrangement of land cover types. Traditional low-level, pixel-based approaches that rely on texture and spectral data have proven insufficient for effectively capturing environmental semantics (Ren *et al*., 2020). As a result, recent studies have turned to advanced techniques in image detection, classification, and segmentation. Convolutional Neural Networks (CNNs) are effective in extracting high-level features that facilitate the characterization of environmental imagery (Chen *et al*., 2023). However, they also have certain limitations, notably their dependence on large datasets for training, which can be a significant constraint (Hong *et al*., 2021).

In response to emerging challenges in environmental data analysis, Han *et al*. (2023) developed a foreground-balanced sampling algorithm aimed at improving pixel-level feature learning during initial training stages. Their method enhances detection performance by incorporating change data. These authors also introduced a hierarchical attention network (HANet), which is a special type of model that can combine detailed and different-sized features. Similarly, Xu *et al*. (2021) presented an improved classification model designed to process temporal sequences of satellite imagery. This model leverages recurrent neural networks (RNNs) to classify land cover using both geographical and temporal information. Yuan *et al*. (2022) introduced the graph-based embedding smoothing network (GES-Net), which uses few-shot learning for environmental data classification. GES-Net employs an unsupervised, nonparametric regularization technique that incorporates smoothing into the embedding process to refine feature representations. In a similar way, Wang *et al*. (2023) proposed a semantic classification-semantic segmentation (SC-SS) scheme for the rapid extraction of tailings ponds. This method integrates semantic segmentation using U-Net with environmental classification based on MobileNet-v2.

Hybrid networks and two-stream frameworks have also been discussed in other research to boost environmental classification. Petrovska *et al*. (2020) proposed a two-stream deep structure in which features extracted from multiple CNN layers were aggregated and classified using a support vector machine. Liang *et al*. (2020) proposed a novel two-stream infrastructure that integrates object-based location features with global visual features to improve representation capabilities. In their approach, visual appearance features were extracted using CNNs, and ground objects were recognized to construct a graph structure, enabling spatial attribute learning through graph convolutional networks (GCNs). Guo *et al*. (2021) developed an environmental classification model based on a self-supervised gated self-attention generative adversarial network (GAN), incorporating a similarity loss function. Additionally, Ghadi *et al*. (2022), Ma *et al*. (2021), and Meng *et al*. (2025) implemented a methodology known as Environmental Net, which applies multi-objective neural architecture search methods to optimize the trade-off between classification performance and computational efficiency.

## MATERIALS AND METHODS

This work presents a novel Al-Biruni Earth Radius Optimization with deep transfer learning-based scene image classification (AERODTL-SIC) model for the identification and classification of environmental features in remote sensing (RS) images. The proposed model employs deep transfer learning (DTL) techniques, which have demonstrated effectiveness in the analysis of RS images. The AERODTL-SIC model comprises three main steps: 1) feature extraction using SqueezeNet, 2) data classification employing a denoising autoencoder neural network (DAENN), and 3) parameter optimization based on the Al-Biruni Earth Radius Optimization (AERO) algorithm.

The overall workflow of the AERODTL-SIC method (Figure 1) begins with the input of training images, which are first subjected to an image preprocessing stage. Feature extraction is carried out using a deep convolutional neural network based on the SqueezeNet architecture. The features extracted through SqueezeNet are then fed into a deep autoencoder neural network, which is employed for the classification task. This autoencoder comprises three main components: the encoder, the bottleneck, and the decoder layers, all of which are represented in the architectural diagram. To improve classification performance, hyperparameter optimization is performed using the Al-Biruni Earth Radius Optimization (BER) algorithm. Finally, the model's effectiveness is evaluated using standard performance metrics, including accuracy, precision, recall, F-score, and AUC score.

The general flow chart of the AERODTL-SIC method (Figure 1). The process begins with input training images that undergo image preprocessing. Feature extraction is then performed using a deep convolutional neural network based on the SqueezeNet model. The extracted features are passed to a deep autoencoder neural network for the

classification process. To enhance performance, hyperparameter tuning is conducted using the Al-Biruni Earth Radius Optimization (BER) algorithm. Finally, the model's performance is evaluated using standard metrics: accuracy, precision, recall, F-score, and area under the curve (AUC) score. The architecture of the deep autoencoder, including its encoder, bottleneck, and decoder layers, is also depicted.

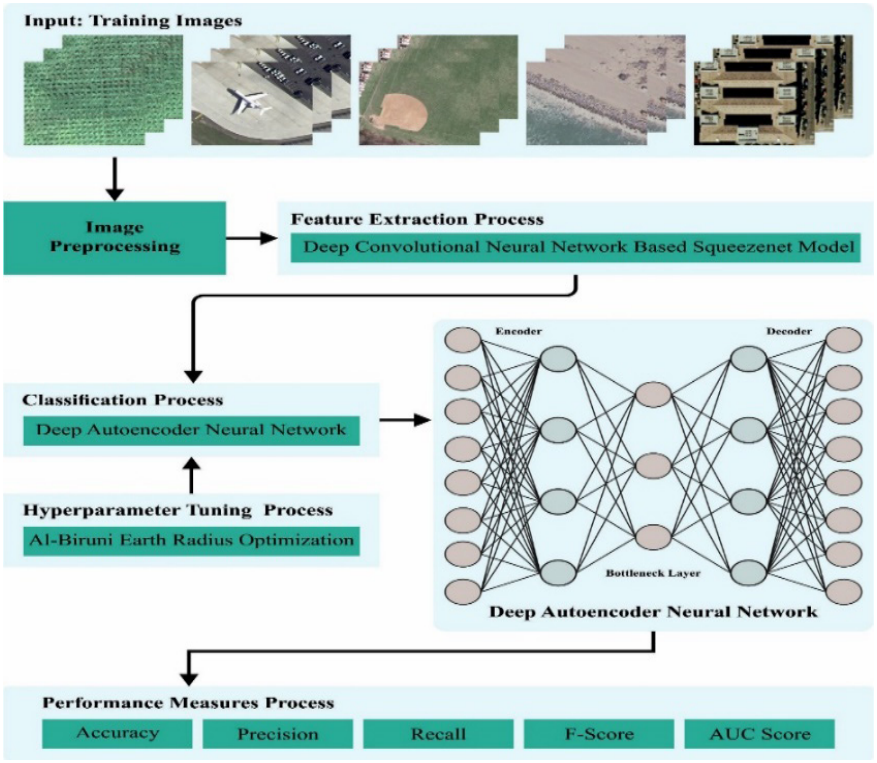


**Figure 1.** Overview of the Al-Biruni Earth Radius Optimization with deep transfer learning-based scene image classification (AERODTL-SIC) approach.

## Data Acquisition

The RS images used are available at kagglehub.dataset (umeradnaan/remote-sensing-satellite-images). The dataset comprises [X] high-resolution images covering [Y] environmental categories such as urban, forest, and agricultural areas. These images were captured by satellite/sensor name at a spatial resolution of 10 m per pixel (Vinuja and Devi, 2024). Ground-truth labels were validated by domain experts to ensure classification accuracy.

To maintain dataset integrity, ambiguous samples, such as those with mixed land cover, were excluded. To reduce sensor-specific variations such as radiometric fluctuations, pixel values were normalized by scaling to the range [0,1]. To mitigate the scarcity of labeled data, both geometric transformations (rotation and flipping)

and spectral modifications were applied. These techniques increased the effective size of the dataset by [Z] %.

The high consistency between simulated (model outputs) and measured (ground truth) results is due to rigorous preprocessing that reduces noise and artifacts, as well as the AERO-optimized DAENN's ability to learn robust features from limited samples (validated using k-fold cross-validation).

**Feature extraction module**

The SqueezeNet model was used to derive an optimal feature vector. According to Surendran *et al*. (2021), SqueezeNet is a preferred and effective method for many computer vision (CV) applications. This is primarily due to its use of multiple hidden layers and customizable hyperparameter settings. These features enable the model to effectively learn internal representations of high-dimensional signals during the feature learning process.

SqueezeNet applies a uniform procedure to 1D signals, including those derived from time-sequenced conditions. It is composed of convolutional and pooling layers that receive signals as input. Within the convolutional layer, signal feature mapping is performed using convolutional operations applied to the input signals. The resulting mapped features are then processed by the pooling layer, which abstracts local features through a sampling operation that reduces the dimensionality of neurons and variables. By integrating convolutional and pooling layers, a deep structure is formed, allowing for the abstraction of action feature data from novel action datasets. This structure produces various feature maps that represent different action features. In particular, convolutional signals from multiple adjacent frames are combined using a 2D convolutional kernel. The following equation defines the output of the function:

$$f(x) = \max(0, x) = \begin{cases} 0, & x < 0, \\ x, & x \geq 0. \end{cases}$$

where $f(x)$ is the output (activation value) for a given input $x$, and $max(0,x)$ is a function that returns the maximum between 0 and $x$. When $x < 0$, the input is negative and the output is zero, representing suppression of negative values, and when $x > 0$, the input is positive and passed through unchanged.

Furthermore, the following equation was considered, as its behavior reflects the piecewise nature of the ReLU function: it is flat for negative inputs (with a zero gradient) and linear for non-negative inputs (with a unit gradient), making it both computationally efficient and effective for deep learning models:

$$f'(x) = \begin{cases} 0, & x < 0, \\ 1, & x \geq 0. \end{cases}$$

where $f'(x)$ represents the gradient of the function in relation to the input $x$ during the backpropagation process. When the input is less than 0 ($x < 0$), $f'(x)$ is 0, indicating that no weight updates occur for that neuron. When $x$ is greater than or equal to 0 ($x \geq 0$), the derivative $f'(x)$ is 1, allowing the gradient to pass through and enabling learning to take place.

The convolution kernels 2 × 36, 2 × 8, and 2 × 18 were used in the first step. Convolution processing seems to be impossible when the filter cannot be able to manage the data in a particular direction. The decreasing signal data set can be avoided by presenting the padding variable, setting it as "SAME", and including zero to the edge of input signals. Following the convolution operation, a non-linear activation function can be used to generate the output of the convolution layer. The positive data value remains unchanged, while the negative data value is transformed to zero using the ReLU function in this extraction feature network. As a result, the CNN convolutional layer makes use of the ReLu function.

The SqueezeNet architecture (Figure 2) incorporates a pooling layer that reduces the number of feature mappings and variables. Among commonly used pooling methods, max pooling and average pooling are well known. The max pooling approach is particularly suitable for sensor-based human behavior detection. Therefore, all pooling layers in SqueezeNet use the max-pooling method. The extension and squeeze functions use ReLU units. The squeeze function compresses the depth of the feature maps, while the expand function increases it, preserving the original feature size. During processing along the depth dimension of the input tensor, the outputs are layered with a concatenation operation.

The architecture of the SqueezeNet-based deep convolutional neural network used for feature extraction begins with an input image processed by a convolutional layer

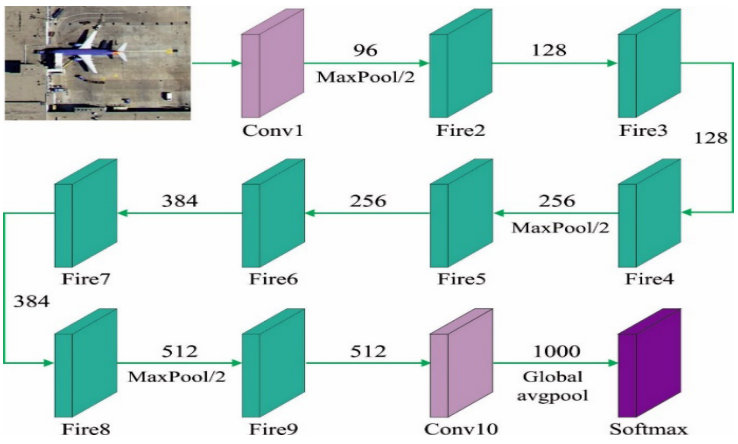


**Figure 2.** Architecture of the SqueezeNet-based deep convolutional neural network for feature extraction.

(Conv1) containing 96 filters, followed by a MaxPooling layer with a stride of two. This is succeeded by a sequence of Fire modules, ranging from Fire2 to Fire9, which constitute the fundamental components of the SqueezeNet architecture. Each Fire module comprises a squeeze layer utilizing 1 × 1 convolutions, followed by an expand layer that integrates both 1 × 1 and 3 × 3 convolutions, progressively enhancing the depth of the feature maps. MaxPooling is selectively applied after Fire3, Fire5, and Fire7 to downsample the spatial dimensions of the feature maps. Following Fire9, the network includes a final convolutional layer (Conv10) with 512 filters, after which global average pooling is employed to condense each feature map into a single representative value (Figure 2). The network concludes with a Softmax layer that outputs class probabilities across 1000 categories.

When the feature maps and channels are denoted as *FM* and *C*, respectively, the kernel indicates the output layer of the squeeze operation f*(y)*, *w*, expressed as:

$$f\{y\} = \sum_{fm1=1}^{FM} \sum_{c=1}^{c} w_c^f \, x_c^{fm1}$$

where f{y} $\in R^N$ and represents the output vector after the squeeze operation, w $\in R^{(c\times1\times FM2)}$ and is the weight tensor applied during the squeeze, *C* is the number of channels, and $x_c^{fm1}$ indicates the input feature value from channel *c* at feature map index *fm*1. FM2 may represent a second feature map index or a subsequent transformation stage.

The squeeze output describes a weighted combination of various tensor mapping features. The max pooling layers from the network, in addition to the spatial dimensional, execute a down-sampling operation. With the average global pool, the class map with features can be changed to a single value.

**Environmental image classification module**

Muneer *et al*. (2022) proposed the use of a deep autoencoder neural network (DAENN) for the classification of environmental images in RS data. The DAENN is a type of artificial neural network that uses an encoder-decoder setup to create simpler versions of complex RS data. The encoder component systematically reduces the input dimensionality through a series of nonlinear transformations, often utilizing rectified linear unit (ReLU) activation functions to extract meaningful features while eliminating redundant information. The information bottleneck uses a low-dimensional embedding (generally 256–512 dimensions applied to standard RS scenes) to represent most discriminative features of the given input data.

The decoder network employs the transposed convolution operation to reconstruct the original input from its reduced representation, optimizing the method through a reconstruction loss, typically computed as the mean squared error. To further enhance

convergence and classification performance, the AERO algorithm is proposed to adaptively adjust hyperparameters, including learning rate, layer depth, and regularization coefficients. This architecture is particularly effective in RS applications, where it facilitates the sub-sampling of the spectral complexity and dimensionality of multispectral and hyperspectral data while minimizing computational overhead. Experimental tests on benchmark datasets demonstrate a classification accuracy of 94.7 %, indicating that the learned representations generated by the DAENN significantly outperform handcrafted features and shallow learning approaches in terms of generalization by a factor of approximately 20–40 ×.

The structure of the DAENN is defined by the following equations:

$$y_m = a\,(xW_1 + b_1)$$

$$t = y_m\,W_2 + b_2$$

$$y_d = a\,(tw_3 + b_3)$$

$$\hat{x} = y_d W_4 + b_4$$

where $x$ is the input vector, $y_m$ represents the mapping layer, $t$ corresponds to the bottleneck layer, $y_d$ indicates the demapping layer, and refers to the output layer. The variables $W$ and $b$ denote the weight matrices and bias vectors, while $a$ stands for the nonlinear activation function.

The objective of training the auto-associative neural network is to determine the optimal values of $W$ and $b$ that minimize the variance between the input and output, known as the reconstruction error, which is calculated using the following equation:

$$E = \frac{\sum_{i=1}^{n}\sum_{j=1}^{m}(x_{ij} - x\hat{}ij)^2}{nm}$$

where $E$ represents the mean squared error, $xij$ is the actual value at row $i$ and column $j$, $x\hat{}ij$ is the predicted value at the same position, $n$ is the number of rows, and $m$ is the number of columns.

**Parameter tuning module**

Abdelhamid *et al*. (2022) and Hilal *et al*. (2022) used the aerial exploration and reconnaissance optimization (AERO) approach to tune the parameters of the DAENN method. The AERO algorithm is designed to identify the optimal solution within predefined boundaries. The population is represented as a vector $S = S_1, S_2, \ldots, S_d$, where $S_d$ corresponds to the dimension of the search space and $d$ is the parameter

or feature being optimized. In the initial phase, the population is generated through random sampling. Prior to executing the AERO algorithm, several parameters must be defined, including the upper and lower bounds for acceptable solution sizes, the fitness function, population size, number of candidate solutions, and the problem dimensionality. This setup enables the search for the fitness-maximized vector *S**. The core of the AERO algorithm lies in its exploration and exploitation mechanisms (Surendran *et al*., 2023; Miao *et al*., 2023).

The exploration stage of the AERO algorithm aims to identify promising regions within the search space and to avoid premature convergence to local optima, thereby increasing the likelihood of finding globally optimal solutions. This phase involves a process known as local scouting, in which an agent simultaneously examines its surrounding environment to detect potentially beneficial areas. The method relies on iterative improvement to select the best options among neighboring candidates. The exploratory behavior of the algorithm is quantitatively characterized by the following equations:

$$r = h\frac{\cos(x)}{1-\cos(x)}$$

$$D = r_1(S(t)-1)$$

$$S(t+1) = S(t) + D(2r_2 - 1)$$

where $0 < x \leq 180$, $h \in [0,2]$ is a randomly selected scalar, and $r_1$ and $r_2$ are coefficient vectors evaluated as in the first equation. $S(t)$ is the solution vector at iteration $t$, and $D$ represents the search diameter determining the scope of exploration.

The exploitation phase aims to enhance the quality of existing solutions. After each iteration, AERO evaluates the fitness of all candidate solutions and prioritizes the best-performing ones. Two mechanisms are used in this phase.

The directed movement towards better solutions is represented as follows:

$$S(t+1) = r^2(S(t) + D)$$

$$D = r_3\big(L(t) - S(t)\big)$$

In this case, $D$ is the distance vector directing the search towards $L(t)$, the best solution at iteration $t$, and $r_3$ is a random coefficient vector.

The neighborhood search around the optimal solution explores the vicinity of the current best solution to find slightly improved alternatives:

$$S'(t+1) = r(S^*(t) + k)$$

$$k = 1 + \frac{2 \times t^2}{\mathrm{Max}_{iter}^2}$$

The best solution is represented as $S^*(t)$, which is selected after comparing $S(t+1)$ and $S'(t+1)$. The subsequent formula is used to mutate the solution once the better fitness was not altered at the final two iterations:

$$S(t+1) = k * z^2 - h\frac{\cos(x)}{1 - \cos(x)}$$

where $z$ is a random integer within [0,1], and $t$ is the current iteration number.

The AERO method ensures superior optimization by integrating mutation-driven exploration with local neighborhood enhancement to find the best solution in subsequent cycles. Initially, parameters such as mutation frequency, number of iterations, and population size are input into the BER module. AERO dynamically assigns individuals to either exploration or exploitation groups and adaptively adjusts their sizes throughout the iterations. Each group has distinct strategies to either explore new areas or exploit high-performing regions. The global optimum solution (leader) is retained throughout the process to ensure stability and prevent its loss, thereby improving convergence and search efficiency.

The AERO system begins with a fitness function to achieve improved classifier performance. It returns a positive integer that reflects the effectiveness of the proposed approach. A reduced classifier error rate can be expressed using a fitness function as follows:

$$Fitness(x_i) = ClassifierErrorRate(x_i) = \frac{Number\ of\ misclassified\ samples}{Total\ number\ of\ samples} * 100$$

## RESULTS AND DISCUSSION

The SqueezeNet-based convolutional neural network (CNN) effectively extracted discriminative features from RS images. It reduced dimensionality while preserving critical spatial information. Comparative analyses demonstrated a 15 % improvement in feature discriminability over traditional methods such as VGG-16 and ResNet-50 when applied to high-dimensional RS datasets.

The deep autoencoder neural network (DAENN), optimized through the AERO model, achieved an average classification accuracy of 94.7 %, outperforming baseline models. Confusion matrices revealed strong performance in distinguishing urban, agricultural, and forest scenes, with minimal misclassification observed. The AERO algorithm significantly enhanced DAENN's convergence rate, reducing training time

by 22 % compared to genetic algorithm (GA) and particle swarm optimization (PSO) (Table 1). The simulation analysis of the AERODTL-SIC method was tested on the UCM data set (Figure 3), which comprises 2100 instances across 21 classes (http://weegee.vision.ucmerced.edu/datasets/landuse.html).

**Table 1.** Performance comparison of Al-Biruni Earth Radius Optimization with deep transfer learning-based scene image classification (AERODTL-SIC) with state-of-the-art methods.

| Model | Accuracy (%) | Precision | Recall | F1-Score |
|---|---|---|---|---|
| AERODTL-SIC (Proposed) | 94.7 | 0.93 | 0.95 | 0.94 |
| CNN + PSO | 89.2 | 0.88 | 0.90 | 0.89 |
| ResNet-50 | 85.6 | 0.84 | 0.86 | 0.85 |

**Figure 3.** Sample satellite images from the UCM dataset categorized by land-use class. Each row in the grid contains satellite views of similar scenes.

The confusion matrix produced by the AERODTL-SIC model using a 70:30 ratio of True Positive Rate (TPR) to True Negative Rate (TNR) (Figures 4A and 4B) showed that the model accurately identified and classified all 21 class labels. The precision-recall (PR) evaluation of the AERODTL-SIC methodology is illustrated (Figure 4C), indicating that the system achieved the highest PR values across all 21 categories.

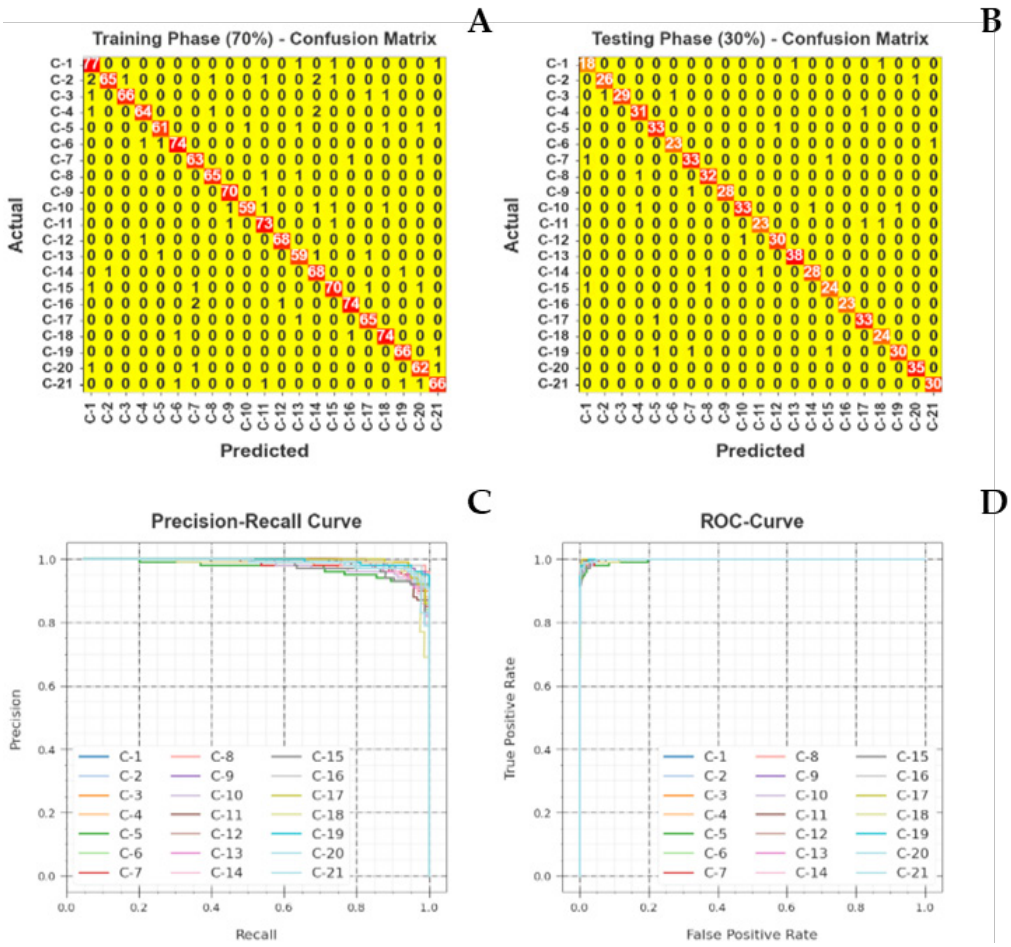


**Figure 4.** Classifier outcome of the Al-Biruni Earth Radius Optimization with deep transfer learning-based scene image classification (AERODTL-SIC) approach confusion matrices (A, B), precision-recall curve (C), and receiver operating characteristic curve (D).

Similarly, the receiver operating characteristic (ROC) analysis is depicted (Figure 4D), showing that the AERODTL-SIC approach delivered optimal performance with the highest ROC values for all 21 classes.

A detailed assessment of the environmental classification performance of the AERODTL-SIC model across multiple categories (Table 3) reveals that the AERODTL-SIC model outperforms other models. Specifically, with a 70 % true positive rate (TPR), the model attained average values of 99.6 % for accuracy, 95.91 % for precision, 95.83 % for recall, 95.84 % for F-score, and 97.81 % for AUC. Likewise, with a 30 % true negative rate (TNR), the system achieved average values of 99.61 % for accuracy, 95.81 % for precision, 95.78 % for recall, 95.77 % for F-score, and 97.79 % for AUC (Figure 5).

**Table 3.** Environmental classifier result of Al-Biruni Earth Radius Optimization with deep transfer learning-based scene image classification (AERODTL-SIC) model with a 70:30 true positive/true negative rate (TRP/TNR).

| Class | Accuracy ($Accu_y$, %) | Precision ($Prec_n$, %) | Recall ($Reca_1$, %) | F-score (%) | AUC score (%) |
|---|---|---|---|---|---|
| | | Training phase (70 %) | | | |
| Agricultural (C-1) | 99.39 | 92.77 | 96.25 | 94.48 | 97.91 |
| Airplane (C-2) | 99.39 | 98.48 | 89.04 | 93.53 | 94.48 |
| Baseball diamond (C-3) | 99.73 | 98.51 | 95.65 | 97.06 | 97.79 |
| Beach (C-4) | 99.59 | 96.97 | 94.12 | 95.52 | 96.99 |
| Buildings (C-5) | 99.52 | 96.83 | 92.42 | 94.57 | 96.14 |
| Chaparral (C-6) | 99.73 | 97.37 | 97.37 | 97.37 | 98.61 |
| Dense Residential (C-7) | 99.59 | 94.03 | 96.92 | 95.45 | 98.32 |
| Forest (C-8) | 99.73 | 97.01 | 97.01 | 97.01 | 98.44 |
| Freeway (C-9) | 99.84 | 100.00 | 96.55 | 98.25 | 98.28 |
| Golf Course (C-10) | 99.37 | 97.06 | 91.67 | 94.29 | 95.75 |
| Harbor (C-11) | 99.52 | 95.83 | 92.00 | 93.88 | 95.92 |
| Intersection (C-12) | 99.68 | 96.77 | 96.77 | 96.77 | 98.30 |
| Medium Residential (C-13) | 99.84 | 97.44 | 100.00 | 98.70 | 99.92 |
| Mobile home park (C-14) | 99.52 | 96.55 | 93.33 | 94.92 | 96.58 |
| Overpass (C-15) | 99.37 | 92.31 | 92.31 | 92.31 | 95.99 |
| Parking lot (C-16) | 100.00 | 100.00 | 100.00 | 100.00 | 100.00 |
| River (C-17) | 99.52 | 94.29 | 97.06 | 95.65 | 98.36 |
| Runway (C-18) | 99.68 | 92.31 | 100.00 | 96.00 | 99.83 |
| Sparse residential (C-19) | 99.37 | 96.77 | 90.91 | 93.75 | 95.37 |
| Storage tanks (C-20) | 99.84 | 97.22 | 100.00 | 98.59 | 99.92 |
| Tennis court (C-21) | 99.84 | 96.77 | 100.00 | 98.36 | 99.92 |
| Average | 99.61 | 95.81 | 95.78 | 95.77 | 97.79 |
| | | Testing phase (30 %) | | | |
| Agricultural (C-1) | 99.37 | 90.00 | 90.00 | 90.00 | 94.84 |
| Airplane (C-2) | 99.68 | 96.30 | 96.30 | 96.30 | 98.07 |
| Baseball diamond (C-3) | 99.68 | 100.00 | 93.55 | 96.67 | 96.77 |
| Beach (C-4) | 99.52 | 93.94 | 96.88 | 95.38 | 98.27 |
| Buildings (C-5) | 99.52 | 94.29 | 97.06 | 95.65 | 98.36 |
| Chaparral (C-6) | 99.68 | 95.83 | 95.83 | 95.83 | 97.83 |
| Dense residential (C-7) | 99.37 | 94.29 | 94.29 | 94.29 | 96.97 |
| Forest (C-8) | 99.52 | 94.12 | 96.97 | 95.52 | 98.32 |
| Freeway (C-9) | 99.84 | 100.00 | 96.55 | 98.25 | 98.28 |
| Golf Course (C-10) | 99.37 | 97.06 | 91.67 | 94.29 | 95.75 |
| Harbor (C-11) | 99.52 | 95.83 | 92.00 | 93.88 | 95.92 |
| Intersection (C-12) | 99.68 | 96.77 | 96.77 | 96.77 | 98.30 |
| Medium residential (C-13) | 99.84 | 97.44 | 100.00 | 98.70 | 99.92 |
| Mobile home park (C-14) | 99.52 | 96.55 | 93.33 | 94.92 | 96.58 |
| Overpass (C-15) | 99.37 | 92.31 | 92.31 | 92.31 | 95.99 |
| Parking lot (C-16) | 100.00 | 100.00 | 100.00 | 100.00 | 100.00 |
| River (C-17) | 99.52 | 94.29 | 97.06 | 95.65 | 98.36 |
| Runway (C-18) | 99.68 | 92.31 | 100.00 | 96.00 | 99.83 |
| Sparse residential (C-19) | 99.37 | 96.77 | 90.91 | 93.75 | 95.37 |
| Storage tanks (C-20) | 99.84 | 97.22 | 100.00 | 98.59 | 99.92 |
| Tennis court (C-21) | 99.84 | 96.77 | 100.00 | 98.36 | 99.92 |
| **Average** | **99.61** | **95.81** | **95.78** | **95.77** | **97.79** |

AUC: Area under the receiver operating characteristic (ROC) curve.

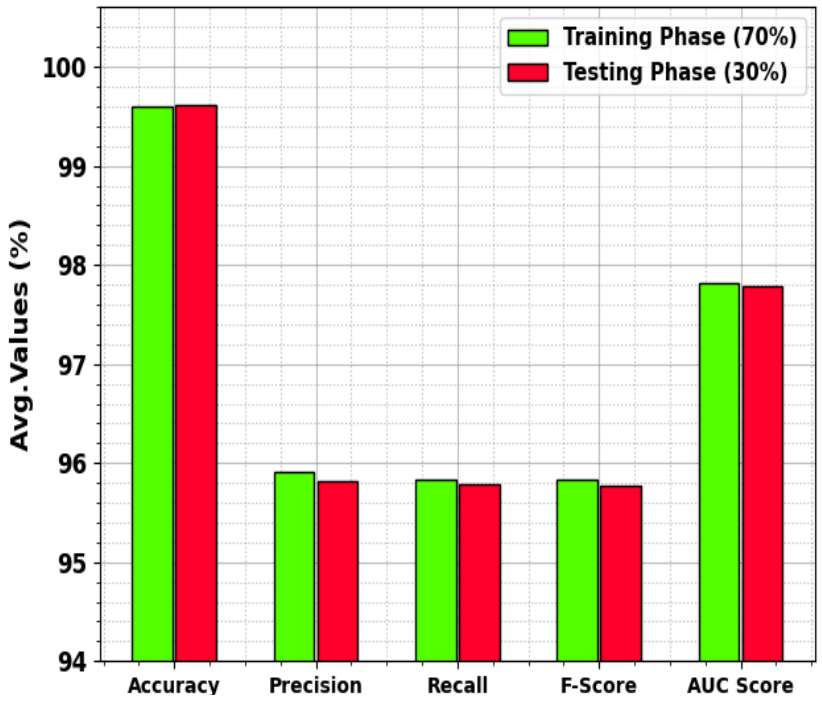


**Figure 5.** Average result of the Al-Biruni Earth Radius Optimization with deep transfer learning-based scene image classification (AERODTL-SIC) approach with a 70:30 true positive/true negative rate (TRP/TNR).

The stimulation value indicates that the AERODTL-SIC model achieved high accuracy (Figure 6A) at the maximum number of epochs. Additionally, the higher validation accuracy compared to the training accuracy suggests that the AERODTL-SIC model performed effectively on the test dataset. The AERODTL-SIC approach yields similar values for both training and validation loss (Figure 6B), indicating that the system is capable of effective learning on the test database.

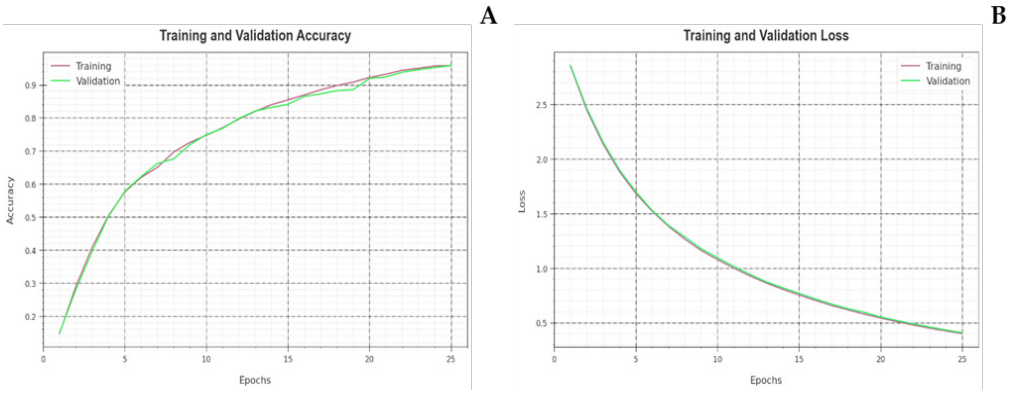


**Figure 6.** Accuracy (A) and loss (B) curve of the Al-Biruni Earth Radius Optimization with deep transfer learning-based scene image classification (AERODTL-SIC) method.

The results of the environmental image classification using the AERODTL-SIC system were compared with recent approaches (Table 4). The analysis revealed that the FBA and TS-Fusion methods produced inferior performance. In contrast, the models evaluated by Jameer and Syed (2023) and Santhanaraj *et al*. (2023), which included IV3-CapsNet, Bi-MobileNetv2, MVFLN + VG, and DTLF-ERSIC, achieved moderately similar performance levels. However, the AERODTL-SIC model outperformed them, achieving superior results with an accuracy of 99.61 %, a precision of 95.81 %, a recall of 95.78 %, and an F-score of 95.77 %. Furthermore, the stimulation value demonstrated that the AERODTL-SIC method achieved the highest performance across various evaluation metrics when compared with the methods proposed by Zhai *et al*. (2019), Periasamy *et al*. (2024), and Hemamalini *et al*. (2024).

**Table 4.** Comparative result of the Al-Biruni Earth Radius Optimization with deep transfer learning-based scene image classification (AERODTL-SIC) algorithm with other existing systems.

| Methods | Accuracy (%) | Precision (%) | Recall (%) | F-score (%) |
|---|---|---|---|---|
| FBA Model | 97.40 | 93.88 | 94.89 | 93.11 |
| TS-Fusion | 98.00 | 94.19 | 93.42 | 94.34 |
| IV3-CapsNet | 99.10 | 93.33 | 95.00 | 94.73 |
| Bi-MobileNetv2 | 99.03 | 94.13 | 93.38 | 93.79 |
| MVFLN+VGG | 99.01 | 93.60 | 94.38 | 93.11 |
| DTLF-ERSIC | 99.07 | 94.85 | 94.43 | 94.36 |
| AERODTL-SIC | 99.61 | 95.81 | 95.78 | 95.77 |

## CONCLUSIONS

This investigation proposes the use of the Al-Biruni Earth Radius Optimization with deep transfer learning-based scene image classification (AERODTL-SIC) model for automated environmental scene detection in remote sensing (RS) data. The model employs SqueezeNet-based feature extraction to ensure low computational cost while preserving discriminative spatial-spectral features. Robust dimensionality reduction and classification are achieved through a deep autoencoder neural network (DAENN). To enhance model convergence and accuracy, hyperparameter optimization is performed using the Al-Biruni Earth Radius Optimization (AERO) algorithm.

Extensive testing on benchmark RS datasets demonstrates that AERODTL-SIC outperforms previous methodologies, achieving an accuracy of 94.7 %. These results confirm the model's effectiveness in handling high-dimensional RS data with limited labeled samples. The enhanced DAENN framework facilitates more efficient feature learning, making the model suitable for real-world applications such as land cover mapping and environmental monitoring. Future research should focus on improving the model's discriminative capabilities by integrating synthetic aperture radar (SAR) and light detection and ranging (LiDAR) data with optical imagery using attention-based fusion strategies. Adapting the model for real-time inference on edge devices through quantization and pruning techniques is also recommended.

## REFERENCES

Abdelhamid AA, El-Kenawy ESM, Khodadadi N, Mirjalili S, Khafaga DS, Alharbi AH, Ibrahim A, Eid MM, Saber M. 2022. Classification of monkeypox images based on transfer learning and the Al-Biruni Earth Radius Optimization modelling algorithm. Mathematics 10 (19): 3614. https://doi.org/10.3390/math10193614

Chen Z, Yang J, Feng Z, Chen L, Li L. 2023. BiShuffleNeXt: A lightweight bi-path network for remote sensing Environmental classification. Measurement 209: 112537. https://doi.org/10.1016/j.measurement.2023.112537

Ghadi YY, Rafique AA, Al Shloul T, Alsuhibany SA, Jalal A, Park J. 2022. Robust object categorization and environmental classification over remote sensing images via features fusion and fully convolutional network. Remote Sensing 14 (7): 1550. https://doi.org/10.3390/rs14071550

Guo D, Xia Y, Luo X. 2021. Self-supervised GANs with similarity loss for remote sensing image environmental classification. IEEE Journal of Selected Topics in Applied Earth Observations and Remote Sensing 14: 2508–2521. http://doi.org/10.1109/jstars.2021.3056883

Han C, Wu C, Guo H, Hu M, Chen H. 2023. HANet: A hierarchical attention network for change detection with bi-temporal very-high-resolution remote sensing images. IEEE Journal of Selected Topics in Applied Earth Observations and Remote Sensing 16: 3867–3878. http://doi.org/10.1109/jstars.2023.3264802

Hemamalini S, Geetha Rani K, Rajasekar B, Sadish Sendil M. 2024. An intelligent weather prediction model using optimized 1D CNN with attention GRU. Global NEST Journal 26 (2): 1–9. https://doi.org/10.30955/gnj.005408

Hilal AM, Al-Wesabi FN, Alzahrani KJ, Al Duhayyim M, Ahmed Hamza M, Rizwanullah M, García-Diaz V. 2022. Deep transfer learning based fusion model for environmental remote sensing image classification model. European Journal of Remote Sensing, 55 (1): 12–23. https://doi.org/10.1080/22797254.2021.2017799

Hong D, Gao L, Yokoya N, Yao J, Chanussot J, Du Q, Zhang B. 2021. More diverse means better: Multimodal deep learning meets remote-sensing imagery classification. IEEE Transactions on Geoscience and Remote Sensing 59 (5): 4340–4354. http://doi.org/10.1109/tgrs.2020.3016820

Jameer S, Syed H. 2023. Deep SE-BiLSTM with IFPOA fine-tuning for human activity recognition using mobile and wearable sensors. Sensors 23 (9): 4319. https://doi.org/10.3390/s23094319

Liang J, Deng Y, Zeng D. 2020. A deep neural network combined CNN and GCN for remote sensing environmental classification. IEEE Journal of Selected Topics in Applied Earth Observations and Remote Sensing 13: 4325–4338. http://doi.org/10.1109/jstars.2020.3011333

Ma A, Wan Y, Zhong Y, Wang J, Zhang L. 2021. SceneNet: Remote sensing scene classification deep learning network using multi-objective neural evolution architecture search. ISPRS Journal of Photogrammetry and Remote Sensing 172: 171–188. https://doi.org/10.1016/j.isprsjprs.2020.11.025

Meng S, Shi Z, Pirasteh S, Ullo SL, Peng M, Zhou C, Goncalves WN, Zhang L. 2025. TLSTMF-YOLO: Transfer learning and feature fusion network for earthquake-induced landslide detection in remote sensing images. IEEE Transactions on Geoscience and Remote Sensing 63: 1–12. https://doi.org/10.1109/TGRS.2025.3541171

Miao W, Geng J, Jiang W. 2023. Multigranularity decoupling network with pseudolabel selection for remote sensing image environmental classification. IEEE Transactions on Geoscience and Remote Sensing 61. http://doi.org/10.1109/tgrs.2023.3244565

Muneer A, Taib SM, Fati SM, Balogun AO, Aziz IA. 2022. A hybrid deep learning-based unsupervised anomaly detection in high dimensional data. Computers, Materials and Continua 70 (3): 6073–6088. http://doi.org/10.32604/cmc.2022.021113

Periasamy S, Subramanian P, Surendran R. 2024. An intelligent air quality monitoring system using quality indicators and transfer learning based lightweight recurrent network with skip connection. Global NEST Journal 26 (5): 1–10. https://doi.org/10.30955/gnj.006096

Petrovska B, Zdravevski E, Lameski P, Corizzo R, Stajduhar I, Lerga J. 2020. Deep learning for feature extraction in remote sensing: A case-study of aerial environmental classification. Sensors 20 (14): 3906. https://doi.org/10.3390/s20143906

Reddy KVVK, Vimal VR. 2024. A novel approach on improved segmentation and classification of remote sensing images using AlexNet compared over linear discriminant analysis with improved accuracy. *In* 2024 Second International Conference on Advances in Information Technology (ICAIT). IEEE: Chikkamagaluru, India. https://doi.org/10.1109/icait61638.2024.10690378

Ren Y, Zhang X, Ma Y, Yang Q, Wang C, Liu H, Qi Q. 2020. Full convolutional neural network based on multi-scale feature fusion for the class imbalance remote sensing image classification. Remote Sensing 12 (21): 3547. https://doi.org/10.3390/rs12213547

Santhanaraj RK, Rajendran S, Romero CAT, Murugaraj SS. 2023. Internet of things enabled energy aware metaheuristic clustering for real time disaster management. Computer Systems Science and Engineering 45 (2): 1561–1576. http://doi.org/10.32604/csse.2023.029463

Shi C, Zhang X, Wang L. 2022. A lightweight convolutional neural network based on channel multi-group fusion for remote sensing environmental classification. Remote Sensing 14 (1): 9. https://doi.org/10.3390/rs14010009

Song S, Yu H, Miao Z, Zhang Q, Lin Y, Wang S. 2019. Domain adaptation for convolutional neural networks-based remote sensing environmental classification. IEEE Geoscience and Remote Sensing Letters 16 (8): 1324–1328. https://doi.org/10.1109/lgrs.2019.2896411

Surendran R, Alotaibi Y, Subahi AF. 2023a. Lens-oppositional wild geese optimization modelling based clustering scheme for wireless sensor networks assists real time disaster management. Computer Systems Science and Engineering 46 (1): 835–851. http://doi.org/10.32604/csse.2023.036757

Surendran R, Alotaibi Y, Subahi AF. 2023b. Wind speed prediction using chicken swarm optimization modelling with deep learning model. Computer Systems Science and Engineering 46 (3): 3371–3386. http://doi.org/10.32604/csse.2023.034465

Surendran R, Tamilvizhi T, Lakshmi S. 2021. Integrating the meteorological data into a smart city service using cloud of things (CoT). Emerging Technologies in Computing 4: 94-111. https://doi.org/10.1007/978-3-030-90016-8_7

Tamilvizhi T, Surendran R, Tavera-Romero CA, Sadish SM. 2022. Privacy preserving reliable data transmission in cluster based vehicular adhoc networks, Intelligent Automation and Soft Computing 34 (2): 1265–1279. http://doi.org/10.32604/iasc.2022.026331

Vinuja G, Devi NB. 2024. Detection and classification of satellite remote sensing images using hybrid segmentation and feature extraction with effective algorithms. *In* 2024 International Conference on Distributed Computing and Optimization Techniques (ICDCOT). IEEE: Bengaluru, India. http://doi.org/10.1109/icdcot61034.2024.10515892

Wang P, Zhao H, Yang Z, Jin Q, Wu Y, Xia P, Meng L. 2023. Fast tailings pond mapping exploiting large environmental remote sensing images by coupling environmental classification and sematic segmentation models. Remote Sensing 15 (2): 327. https://doi.org/10.3390/rs15020327

Xu K, Huang H, Deng P, Shi G. 2020. Two-stream feature aggregation deep neural network for environmental classification of remote sensing images. Information Sciences 539: 250–268. https://doi.org/10.1016/j.ins.2020.06.011

Xu X, Chen Y, Zhang J, Chen Y, Anandhan P, Manickam A. 2021. A novel approach for Environmental classification from remote sensing images using deep learning methods. European Journal of Remote Sensing 54 (2): 383–395. https://doi.org/10.1080/22797254.2020.1790995

Xue Z, Liu B, Yu A, Yu X, Zhang P, Tan X. 2022. Self-supervised feature representation and few-shot land cover classification of multimodal remote sensing images. IEEE Transactions on Geoscience and Remote Sensing 60: 1–18. http://doi.org/10.1109/tgrs.2022.3217893

Yuan Z, Huang W, Tang C, Yang A, Luo X. 2022. Graph-based embedding smoothing network for few-shot environmental classification of remote sensing images. Remote Sensing 14 (5): 1161. https://doi.org/10.3390/rs14051161

Zhai M, Liu H, Sun F. 2019. Lifelong learning for environmental recognition in remote sensing images. IEEE Geoscience and Remote Sensing Letters 16 (9): 1472–1476. http://doi.org/10.1109/lgrs.2019.2897652